# Process-Level Modelling and Optimization to Evaluate Metal-Organic Frameworks for Post-Combustion Capture of CO2

| | |
|---|---|
| Complete List of Authors: | Yancy Caballero, Daison; Northwestern University, Department of Chemical and Biological Engineering<br>Leperi, Karson; Northwestern University, Department of Chemical and Biological Engineering<br>Bucior, Benjamin; Northwestern University, Department of Chemical and Biological Engineering<br>Richardson, Rachelle; NuMat Technologies<br>Islamoglu, Timur; Northwestern University, Department of Chemistry<br>Farha, Omar; Northwestern University, Department of Chemistry<br>You, Fengqi; Cornell University,<br>Snurr, Randall; Northwestern University, Department of Chemical & Biological Engineering |
| | |

SCHOLARONE™
Manuscripts

# Molecular Systems Design & Engineering

## ARTICLE

## Design, System, Application

Metal-organic frameworks (MOFs) are attractive adsorbent materials for carbon capture applications due to their high capacity for $CO_2$ and tunability. MOF screening is generally performed either by inspecting the isotherms or by using derived adsorbent metrics such as the working capacity, the selectivity, and other figures of merit and performance indicators. However, these metrics do not consider inherent aspects of the process such as the adsorption dynamics and temperature variations, which could shift the adsorption equilibrium and affect the performance of MOFs in pressure swing adsorption (PSA) cycles. In this work, we use a rigorous PSA model along with optimization tools to perform economic analysis and investigate a set of 15 MOFs that have been suggested as promising for carbon capture in the literature. We ranked the MOFs for several PSA cycle configurations based on their economic performance and compared these ranked lists with a ranking based on the derived metrics. Such a comparison suggests that some metrics can lead to misleading results in the adsorbent performance. According to the economic analysis, UTSA-16, Cu-TDPAT, Zn-MOF-74, Ti-MIL-91, and SIFSIX-3-Ni were optimal candidates for post-combustion carbon capture. Our results confirm that including detailed process modelling and optimization in the screening adsorbent workflow is critical for the design and selection of MOF adsorbents.

# Molecular Systems Design & Engineering

## Process-Level Modelling and Optimization to Evaluate Metal-Organic Frameworks for Post-Combustion Capture of CO$_2$

Daison Yancy-Caballero,[a] Karson T. Leperi,[a] Benjamin J. Bucior,[a] Rachelle K. Richardson,[d] Timur Islamoglu,[b] Omar K. Farha,[a,b] Fengqi You,[*c] and Randall Q. Snurr[*a]

Many metal-organic framework (MOF) materials have been reported in the literature as promising for carbon capture applications based on isotherm data or simple adsorbent metrics. However, adsorption process conditions are often neglected in these evaluations. In this study, we performed process-level simulation and optimization of pressure swing adsoprtion processes on a set of promising MOFs reported in the literature for post-combustion carbon capture. Zeolite 13X was also included as a benchmark material. We examined the ability of the MOFs to achieve the Department of Energy goals of 90% CO$_2$ purity and 90% CO$_2$ recovery by employing process-level optimization using three different cycle configurations: a modified Skarstrom cycle, a five-step cycle, and a fractionated vacuum swing adsorption cycle. Then, we ranked the MOFs based on their economic performance by looking at the productivity and energy requirements for each cycle. We compared this ranking of the MOFs with the rankings provided by other metrics and found that the adsorbent rankings suggested by simplified metrics may differ significantly from the rankings predicted by detailed process optimization. The economic optimization analysis suggests that the best performing MOFs from those analyzed here are UTSA-16, Cu-TDPAT, Zn-MOF-74, Ti-MIL-91, and SIFSIX-3-Ni. Looking at the connection between process performance and material propertries, we found that high CO$_2$ working capacity, small pore size, and large difference between the heat of adsorption of CO$_2$ and N$_2$ promote CO$_2$ capture ability based on this small data set. We synthesized one of the top performing MOFs, SIFSIX-3-Ni, and measured its CO$_2$ and N$_2$ adsorption isotherms. The measured isotherms allowed us to estimate the N$_2$ heat of adsorption for SIFSIX-3-Ni, which was not previously available and was required for the process-level modelling.

## Design, System, Application

Metal-organic frameworks (MOFs) are attractive adsorbent materials for carbon capture applications due to their high capacity for CO$_2$ and their tunability. MOF screening is generally performed either by inspecting the isotherms or by using derived adsorbent metrics such as the working capacity, the selectivity, and other figures of merit and performance indicators. However, these metrics do not consider inherent aspects of the process such as the adsorption dynamics and temperature variations, which could shift the adsorption equilibrium and affect the performance of MOFs in pressure swing adsorption (PSA) cycles. In this work, we use a rigorous PSA model along with optimization tools to perform economic analysis and investigate a set of 15 MOFs that have been suggested as promising for carbon capture in the literature. We ranked the MOFs for several PSA cycle configurations based on their economic performance and compared these ranked lists with a ranking based on the derived metrics. Such a comparison suggests that some metrics can lead to misleading results in the adsorbent performance. According to the economic analysis, UTSA-16, Cu-TDPAT, Zn-MOF-74, Ti-MIL-91, and SIFSIX-3-Ni were optimal candidates for

[a.] Department of Chemical and Biological Engineering, Northwestern University, Evanston, IL 60208 USA.
[b.] Department of Chemistry, Northwestern University, Evanston, IL 60208 USA.
[c.] Robert Frederick Smith School of Chemical and Biomolecular Engineering, Cornell University, Ithaca, NY 14853 USA.
[d.] NuMat Technologies, 8025 Lamon Avenue, Skokie, IL 60077, United States

* Correspondence concerning this article should be addressed to R.Q. Snurr at snurr@northwestern.edu and F. You at fengqi.you@cornell.edu

post-combustion carbon capture. Our results confirm that including detailed process modelling and optimization in the screening adsorbent workflow is critical for the design and selection of MOF adsorbents.

## Introduction

Carbon capture and sequestration (CCS) can significantly reduce the $CO_2$ emissions from existing coal- and gas-fired power plants. CCS is composed of three steps: 1) capture of $CO_2$ from a point source, 2) compression and transport of the captured $CO_2$, and 3) storage of $CO_2$ in geological formations. Adsorption-based processes are attractive for the capture step, as they tend to have lower costs than other traditional separation methods.[1] To lower the expected costs of $CO_2$ capture, it is necessary to develop high performance adsorbent materials and to optimize the separation process in which those materials are used.

The choice of adsorbent plays an essential role in adsorption-based carbon capture.[2] Metal-organic frameworks (MOFs) are a class of adsorbent materials that have attracted significant interest over the last few decades due to their high capacity for various gases and their tunability for different applications. Thousands of MOFs have been synthesized for a variety of applications, such as gas separation and storage,[3–5] catalysis,[6,7] and destruction of chemical warfare agents.[8,9] Over the years, numerous MOFs have been synthesized and reported as promising for CCS applications.[10] In general, MOFs are reported as promising for CCS based on high $CO_2$ working capacity or high $CO_2/N_2$ selectivity at adsorption conditions without considering the process conditions or the cycle configuration in which the material would be used.[11–13]

Since there is often a tradeoff between the working capacity and selectivity, other derived metrics have been proposed for preliminary evaluation of adsorbents for pressure swing adsorption (PSA). Metrics such as the PSA sorbent selection parameter,[14] the adsorbent figure of merit,[14,15] the adsorbent performance indicator,[16] and the separation factor[17] require only equilibrium adsorption isotherms as inputs. Most of these metrics incorporate the working capacities and selectivities at adsorption and desorption conditions, and some, such as the adsorbent performance indicator proposed by Wiersum et al.,[16] also include the heat of adsorption of $CO_2$. Some studies have used these derived metrics to find correlations between separation performance and the structural properties of adsorbents and to guide the design of MOFs with good performance for $CO_2$ capture. Wu et al.[18] used this approach to show that the $CO_2/N_2$ selectivity is highly dependent on the difference of the isosteric heats of adsorption of $N_2$ and $CO_2$ ($\Delta Q_{st}^0$) and the porosity, concluding that increasing $\Delta Q_{st}^0$ and decreasing the porosity is an important design rule to develop top performing MOFs for $CO_2$ capture. Wilmer et al.[19] used derived metrics to analyse the structure-performance relation of 139,000 hypothetical MOFs using molecular simulation to provide the adsorption data. They suggested that the most promising MOFs for $CO_2$ separation from flue gas should have a surface area less than 1000 $m^2/g$, a pore-limiting diameter between 4 Å and 7 Å, a $Q_{st}$ of $CO_2$ between 25 and 40 kJ/mol,

and a porosity between 0.3 and 0.4. Similar results were reported recently by Altintas et al.[20] who screened another MOF database to identify the best materials for $CO_2$ capture. They investigated the relationships between pore size, porosity, surface area, density, lattice structure, metal type, and some of the adsorbent metrics mentioned above.

Many derived metrics have been based on intuition, and their reliability for ranking materials is not well understood. Recently, Leperi et al.[21] ran process-level modeling and optimization on 190 materials and used the results to develop a general evaluation metric (GEM) for evaluating sorbents for $CO_2$ capture by PSA. They studied a fractionated vacuum pressure swing adsorption (FVPSA) cycle for post-combustion $CO_2$ capture. Their GEM requires only the working capacities of $CO_2$ and $N_2$, the selectivity at desorption conditions, and the heat of adsorption of $N_2$ as inputs. Leperi et al.[21] showed that the new metric outperforms other metrics reported in the literature for ranking MOFs in terms of the cost of $CO_2$ capture and ability to meet purity and recovery goals. Another metric for PSA that was derived from process-level modeling was presented by Balashankar et al.[22] They reported a classification metric based on process optimization of a vacuum swing adsorption (VSA) cycle to identify adsorbents satisfying purity and recovery constraints. They also presented and validated an approach to estimate the process energy consumption. With the presented metrics, they screened thousands of adsorbents, including those in the NIST/ARPA-E adsorbent database,[23] and identified the MOFs USTA-16 and $[NC_2H_8]4Cu_5$-$(BTT)_3xG$, the zeolite GIS, and the microporous organic polymer C24H21N3, as promising materials for post-combustion carbon capture in terms of minimum energy requirements.

The integration of process modelling and economic optimization directly into the screening of adsorbent materials is an alternative approach that could be attractive.[21,24–28] Process modelling and optimization for PSA requires solving complex and coupled algebraic and partial differential equations, so evaluating a larger number of materials may require considerable computing resources. However, process optimization is needed to account for the effects of the cycle configuration, the dynamics of adsorption, and heat transfer and to guarantee that purity and recovery requirements are satisfied. Following this approach, Maring et al.[11] proposed a simplified model of a VSA cycle to evaluate the performance of four different adsorbents in post-combustion $CO_2$ capture. In this study, Maring et al.[11] suggested an optimal value of the heat of adsorption of $CO_2$ between 35 and 45 kJ/mol and claimed that the $N_2$ heat of adsorption is less important when evaluating the performance in a $CO_2$ capture process. They also determined that the surface area has a limit beyond which an increase is detrimental for the performance and that existing metrics to evaluate adsorbent performance can be misleading because these metrics do not account for thermal effects. Danaci et al.[26] evaluated 25 different adsorbents among MOFs, zeolites, and activated carbon for different $CO_2$ capture

scenarios in a three-step VSA cycle using performance constraints ($CO_2$ purity, $CO_2$ recovery, and cost). Danaci *et al.* included detailed economic modelling as an important aspect in the performance evaluation of a material, using a simplified process model (0-D equilibrium model) that assumed that the adsorbed phase is always at equilibrium with the gas phase. Using their method, they reported that UTSA-16 was the most performing MOF for post combustion capture, while Mg-MOF-74 performed poorly.

In the same context, Rajagopalan *et al.*[24] employed process optimization on a 4-step PSA cycle with light product pressurization to evaluate the performance of four different adsorbents (Mg-MOF-74, UTSA-16, zeolite 13X, and a specific coconut shell activated carbon) for post-combustion carbon capture in terms of productivity and energy consumption. The cycle configuration chosen in this work was shown previously to have advantages for low energy requirements in post-combustion $CO_2$ capture.[29,30] Rajagopalan *et al.*[24] evaluated the efficacy of several PSA metrics by comparing these with their process optimization results. They found that most traditional metrics work fairly well in identifying the poor performance of the activated carbon. However, all of the tested metrics failed to rank properly the other three studied adsorbents, and results from the metrics were not correlated with the performance that they found in process optimization. One important discovery from their work was the importance of low working capacity of $N_2$ as a good predictor of the process performance. This was also reported by Leperi *et al.*[21]

Balashankar and Rajendran[27] used detailed process optimization of a VSA cycle to screen zeolite materials and identify promising candidates able to reduce the parasitic energy in carbon capture applications. They reported 16 promising zeolites that outperformed zeolite 13X in both productivity and energy consumption and suggested optimal ranges for the heat of adsorption of $CO_2$ (32 to 42 kJ/mol) and $N_2$ (8 to 17 kJ/mol) that minimize energy consumption.

The objective of this work is to use process-level simulation and optimization to investigate the performance of fifteen MOFs that were reported in the literature as promising for post-combustion $CO_2$ capture. Zeolite 13X was also included as a benchmark material for CCS. A novel contribution of this study is that we examined multiple PSA cycle configurations to assess the effect of cycle configuration on the relative performance of the materials. Thus, we first evaluated each MOF in three different cycle configurations (a modified Skarstrom cycle, a five-step cycle, and a fractionated vacuum swing adsorption cycle) to evaluate whether the MOF can achieve the Department of Energy (DOE) goals for CCS of 90% $CO_2$ purity and 90% $CO_2$ recovery. For each MOF that can achieve the goals, we then maximized the productivity and minimized the energy requirements to compare their economic performance in each PSA cycle. We also ranked the selected MOFs by some common metrics reported in the literature and then compared these rankings with the rankings coming from the detailed economic optimization. Performance/structure relationships were also investigated. For the material that was reported to have the highest selectivity, SIFSIX-3-Ni, we measured the $CO_2$ and $N_2$

isotherms at multiple temperatures, so that we could obtain the $N_2$ heat of adsorption, which is needed for process modelling and in some of the derived metrics.

## Methods

### Adsorbent Isotherm Fitting

For this study, experimental $CO_2$ and $N_2$ isotherms along with heat of adsorption data were gathered for the 15 MOFs listed in Table 1, along with zeolite 13X. The isotherms were obtained from the literature, except those for the SIFSIX-3-Ni, which were obtained as a part of this work. For all MOFs, the pure-component $CO_2$ isotherms were fitted to the dual-site Langmuir model, and the pure-component $N_2$ isotherms were fitted to the single-site Langmuir model.[29] The isotherm parameters are presented in Table S3, and the fitted isotherms in the pressure range used in optimization along with the experimental data for all adsorbents are presented in Figures S1-S15.

To model the competitive isotherms of the two gases, we assumed that the stronger adsorbing $CO_2$ site, designated as site 1, only adsorbs $CO_2$, while $CO_2$ and $N_2$ compete for the weaker site 2:

$$q_{CO_2}^* = \frac{q_{sat,CO_2}^1 \cdot B_{CO_2}^1 \cdot P_{CO_2}}{1 + B_{CO_2}^1 \cdot P_{CO_2}} + \frac{q_{sat,CO_2}^2 \cdot B_{CO_2}^2 \cdot P_{CO_2}}{1 + B_{CO_2}^2 \cdot P_{CO_2} + B_{N_2}^2 \cdot P_{N_2}} \quad (2)$$

$$q_{N_2}^* = \frac{q_{sat,N_2}^2 \cdot B_{N_2}^2 \cdot P_{N_2}}{1 + B_{CO_2}^2 \cdot P_{CO_2} + B_{N_2}^2 \cdot P_{N_2}} \quad (3)$$

where $q_{sat,i}^s$ and $B_i^s$ are the saturation loading and isotherm parameter of component *i* for site *s*, respectively. To account for the temperature effects on the $CO_2$ and $N_2$ loading, Arrhenius equations were fitted for the isotherm parameters:

$$B_i^s = b_i^s exp\left[\frac{-\Delta U_i^s}{RT}\right] \quad (4)$$

where $\Delta U_i^s$ is the internal energy of adsorption of component *i*.

One problem that arose while collecting the isotherm data was the lack of data reported in the MOF literature for the $N_2$ heats of adsorption. While most researchers recognize the importance of $CO_2$ heat of adsorption on the economic feasibility of MOFs for CCS applications and report the data, $N_2$ heat of adsorption data is often not reported. For MOFs with no $N_2$ heat of adsorption data reported, we assumed the heat of adsorption to be 12 kJ/mol, which is a reasonable assumption according to other studies in the literature.[22] To justify this assumption, we performed a sensitivity analysis on the impact that the $N_2$ heat of adsorption has on the maximum $CO_2$ purity and recovery performance of the MOF. The results are reported in Figure S16. We can see that the largest variation in the maximum $CO_2$ purity was for NTU-105, which increased around 14% when varying the $N_2$ heat of adsorption within a reasonable range from 6 to 18 kJ/mol. One important aspect to be highlighted from the sensitivity analysis is that the MOF's ability to achieve the purity and recovery goals did not change with the variation of the $N_2$ heat of adsorption.

## Synthesis of SIFSIX-3-Ni and Sorption Analysis

Pyrazine (72.0 g, 0.90 mol) was added to a solution of nickel nitrate hexahydrate $Ni(NO_3)_2$ 6 $H_2O$ (130.8 g, 0.45 mol) and ammonium hexafluorosilicate $(NH_4)_2SiF_6$ (80.0 g, 0.45 mol) in 400 mL water in a 1-L media bottle. The resulting solution was heated in an oven at 90˚C and allowed to solvothermally react for 48 h. The mother liquor was decanted and the crystalline powder was washed with water (1 x 200 mL) for 1 hour. The powder was then washed with hot methanol (7 x 100 mL) over 5 days. The product was dried under vacuum (0.01 Torr) for 24 h at 150˚C. Finally, 58.26 g of product was obtained with a yield of 35.9%.

To evaluate the sorption behavior, nitrogen and carbon dioxide isotherm measurements at different temperatures were carried out on a Micromeritics ASAP 2020. The sample was activated at 150 °C under vacuum for 24 h on a Micromeritics Smart VacPrep instrument.

## PSA Modelling

The PSA model is composed of a set of partial differential algebraic equations (PDAE) describing mass, energy, and momentum balances, and it is coupled with the linear driving force model, and the dual-site competitive Langmuir isotherm shown in eqs. (1)-(2). The PSA model incorporates the following assumptions for the packed bed column: 1) there is axially dispersed plug flow in the column, 2) the gas phase is represented by the ideal gas law, 2) the gas and the solid phases are in thermal equilibrium, 3) the pressure drop along the column is well described by the Ergun equation, and 4) the void fraction and particle size remain constant along the column. The detailed formulation of the PSA model and the parameters used in simulations and optimizations can be found in the supplementary information, and in our previous work.[31] The PSA model was discretized using the finite volume method with the weighted essentially non-oscillatory (WENO) scheme,[32] and then the resulting ODE system was solved in MATLAB with the ode15s solver.[33] We used a uni-bed approach to simulate the PSA cycles, where the same bed is used to simulate the different steps in the cycle in sequence until cyclic steady state is achieved, when the final conditions (molar loadings, mole fractions, pressure, and temperature) in the last step match the initial conditions in the first step within a tolerance of $10^{-4}$ in the dimensionless variable. In addition, to ensure no accumulation in the column, the ratio of the gas entering the column to the gas exiting the column over the entire cycle needs to match within a tolerance of $5 \times 10^{-3}$. Explicit boundary conditions were imposed to define each PSA step as suggested in the literature.[29] The MATLAB codes used to simulate and optimize the PSA systems using NSGA-II are available on GitHub (https://github.com/PEESEgroup/PSA).

## PSA Cycles

In this study, we considered three cycle configurations: a modified Skarstrom cycle,[34] a fractionated vacuum swing adsorption (FVSA) cycle,[29] and a five-step cycle,[34] as shown in Figure 1. The modified Skarstrom cycle consists of the following

steps: (1) pressurization, (2) adsorption, (3) heavy reflux, (4) counter-current depressurization, and (5) light reflux. The cycle starts with the bed, initially at the low pressure ($P_L$), being pressurized up to the adsorption pressure ($P_H$) using the flue gas feed. After the pressurization step, the top end of the column is opened, and the feed gas is fed through, allowing for the adsorption step, where $CO_2$ is concentrated at the front of the column, while $N_2$ leaves through the other end of the column. After a predetermined time, the gas flowing into the column is switched from the flue gas to heavy product collected during the light reflux step. Since this heavy product has a higher concentration of $CO_2$ than the feed gas, this step further increases the concentration of $CO_2$ at the entrance of the column. At the end of the heavy reflux step, the end of the column is closed, and the pressure at the entrance of the column is dropped to $P_L$ in the counter-current depressurization step. During this step the emissions from the entrance are collected as the $CO_2$ product. Once the bed is fully depressurized, some of the light product produced during the feed step is fed into the top of the column. As mentioned above, a fraction of the heavy product produced in this step is used as the feed gas during the heavy reflux step. While this reflux reduces the amount of $CO_2$ collected during the cycle, it does significantly enhance the maximum $CO_2$ purity that can be achieved with different adsorbents and has been shown in previous investigations to be promising.[34]

The FVSA cycle consists of the following steps: (1) pressurization, (2) adsorption, (3) co-current depressurization, and (4) counter-current depressurization. This cycle begins with the pressurization step, in which the pressure in the column is increased from the lower pressure ($P_L$) to the adsorption pressure ($P_H$) using the flue gas feed. Then, the top of the column is opened, and the adsorption step takes place. After some time, the bottom inlet of the column is closed, and vacuum is pulled from the top of the column, reducing the pressure to an intermediate value ($P_I$) in the co-current depressurization step. This step is used to further remove $N_2$ from the column, increasing the purity of the final $CO_2$ product. Once $P_I$ has been reached, the top of the column is closed, and the pressure at the bottom of the column is dropped back to $P_L$, which is the start of the counter-current depressurization step. It is during this final step that the $CO_2$ is collected.

The five step cycle consists of the following steps: (1) light product pressurization, (2) adsorption, (3) heavy reflux, (4) co-current depressurization, and (5) counter-current depressurization. This cycle starts with the bed being pressurized from the lower pressure ($P_L$) to the adsorption pressure ($P_H$), using the effluent from the adsorption step, which is fed in reverse direction into the top end of the column. After the light product pressurization step, the feeding of the effluent from the adsorption step is interrupted, and the inlet of the column is opened to allow the flue gas to flow into the column in the adsorption step. After that, the gas flowing into the column is switched from the flue gas to the heavy product collected during the counter-current depressurization step, which causes an increase in the $CO_2$ concentration at the entrance of the column. After the heavy reflux step, the inlet of

the column is closed, and vacuum is pulled from the top of the column, reducing the pressure to $P_I$ in the co-current depressurization step, and removing $N_2$ from the column. Finally, the top end of the column is closed, and the pressure at the entrance is further reduced to $P_L$ in the counter-current depressurization step, in which the $CO_2$ is collected.

### Optimization Technique

In analyzing the capabilities of the different adsorbents, it is necessary to optimize the operating parameters of the different PSA cycles to determine the maximum $CO_2$ purity and recovery, along with maximum productivity and minimum energy requirement for each MOF and zeolite. We used the non-dominated sorting genetic algorithm (NSGA-II)[35] for the optimizations of the cycles. In this study, we performed two separate optimizations: process-level optimization and economic-level optimization. For the process-level optimization, we maximized the $CO_2$ purity and recovery to identify the MOFs that can achieve the DOE's goal of 90% $CO_2$ purity and recovery. The $CO_2$ purity and recovery for each cycle configuration are defined as follows:

$$Purity = \frac{\text{Moles of } CO_2 \text{ in the product}}{\text{Total moles in the product}} \times 100\% \qquad (5)$$

$$Recovery = \frac{\text{Moles of } CO_2 \text{ in the product}}{\text{Moles of } CO_2 \text{ fed into the cycle}} \times 100\% \qquad (6)$$

For the process-level optimization, we used a population of 10 times of the total number of decision variables for the NSGA-II algorithm and ran it for 60 generations. The decision variables along with upper and lower bounds are listed in Table 2 for each PSA cycle considered in this study. For the first optimization problem, we were only interested in knowing whether the MOFs can achieve the goal without needing high-level accuracy. Hence, we used a coarse-level discretization for this stage of the optimization, dividing the column into 10 finite volume elements, which was an acceptable number of finite volumes to achieve a fair accuracy in reasonable computation time. The process-level optimization can be formulated as follows:

$$
\begin{aligned}
\max \quad & CO_2 \text{ Purity} \\
\text{s.t.} \quad & \text{PDAE model} \\
& CO_2 \text{ Recovery} \geq 90\% \\
& P_H \geq P_I \\
& P_I \geq P_L \\
& L/D \geq 3 \\
& LB \leq L, P_H, P_I, P_L, t_{feed}, v_{feed}, \alpha_{LR}, \alpha_{HR} \leq UB
\end{aligned}
\qquad (7)
$$

where $P_H$ is the higher or adsorption pressure, $P_L$ is the lower or desorption pressure, $P_I$ is the intermediate pressure used in the co-current depressurization step in the FVSA cycle, LB and UB are lower and upper bounds imposed on the decision variables (see Table 2). $t_{feed}$ and $v_{feed}$ are the time and the inlet velocity of the adsorption ("feed") step, respectively. The L/D constraint was used to avoid excessively large column diameters compared to column length due to practical operation considerations. We also noticed that without imposing this constraint, we obtained large column diameters corresponding

to small values of L/D between 0.7-1.18, which caused a slight decrease in the productivity.

After the MOFs that can achieve the DOE's goals were identified, we performed economic optimization for minimizing the energy requirement and maximizing the productivity. The energy requirement and productivity are calculated as follows:

$$Productivity\left[\frac{\text{mol } CO_2}{\text{kg} \cdot \text{s}}\right] = \frac{\text{Moles of } CO_2 \text{ in the product}}{\text{Mass of adsorbent} \times \text{cycle time}} \qquad (8)$$

$$Energy\ Req.\left[\frac{\text{kWh}}{\text{ton } CO_2}\right] = \frac{\text{Energy required for all steps}}{\text{mass of } CO_2 \text{ collected in the product per cycle}} \qquad (9)$$

The economic optimization was performed in two stages. We first performed a coarse-level optimization, dividing the column into 10 finite volume elements, and ran this optimization for 100 generations with a population of 10 times the number of decision variables. The NSGA-II for this second optimization problem was initialized with the final results from the process-level optimization. After running the coarse-level optimization, we performed a finer level optimization with 30 finite volume elements, initializing with the coarse-level optimization results. We still used a population of 10 times of the total number of decision variables for this optimization, but we ran the NSGA-II for only 30 generations. The economic optimization model can be represented as follows:

$$
\begin{aligned}
\max \quad & \text{Productivity} \\
\min \quad & \text{Energy Requirement} \\
\text{s.t.} \quad & \text{PDAE model} \\
& CO_2 \text{ Purity} \geq 90\% \\
& CO_2 \text{ Recovery} \geq 90\% \\
& P_H \geq P_I \\
& P_I \geq P_L \\
& L/D \geq 3 \\
& LB \leq L, P_H, P_I, P_L, t_{feed}, v_{feed}, \alpha_{LR}, \alpha_{HR} \leq UB
\end{aligned}
\qquad (10)
$$

## Results

### Purity/Recovery Maximization

We first examined the results from maximizing $CO_2$ purity and recovery for the sixteen adsorbents listed in Table 1. The Pareto curves representing the best combination of purity/recovery achievable by each adsorbent are shown in Figure 2 (a-c) for the three different cycles. As seen from the figure, there is a large range in performance among the sixteen adsorbents for each cycle. At the low end of the performance, we can see that MOF-177 and NTU-105 can only purify the $CO_2$ product up to 51% in the five step cycle. For the other two cycles the highest $CO_2$ purity achieved is even lower (see Tables S4, S6, and S8 for the highest $CO_2$ purity achieved for the sixteen adsorbents in the three PSA cycles). As discussed further below, the poor performance of MOF-177 and NTU-105 seems to correlate with their large surface areas (~4600 and ~3500 $m^2/g$, respectively) and low crystal densities (0.43 and 0.59 $g/cm^3$, respectively).[36,37] A large surface area and open pore structure are beneficial for applications that need large saturation capacities at high pressures (such as hydrogen storage) but

hinder the performance of MOF-177 and NTU-105 at the low operating pressure of $CO_2$ capture.

At the other end of the performance spectrum, there are several MOFs that can achieve the $CO_2$ purity goal of 90% while recovering 90% of the $CO_2$. The number of MOFs able to achieve these purity/recovery targets varied with the cycle configuration, with 8 MOFs able to meet the targets for the modified Skarstrom cycle, 5 for the FVSA cycle, and 6 for the five-step cycle. Along with zeolite 13X, which can achieve the goals in all of the studied cycles, we found that UTSA-16, Cu-TDPAT, Ti-MIL-91, Zn-MOF-74, and SIFSIX-Ni-3 met or exceeded the purity and recovery goals in all three cycles. We can see that UTSA-16 outperformed zeolite 13X in all cycles in terms of purity/recovery and that Cu-TDPAT has similar performance to zeolite 13X in the FVSA and five step cycle. In addition to these MOFs, Ni-MOF-74, Mg-MOF-74, and SIFSIX-2-Cu-i were also able to meet the purity and recovery targets in the modified Skarstrom cycle and Mg-MOF-74 in the five step cycle.

In addition to the optimization results presented in Figure 2 that guarantee a minimum $CO_2$ recovery of 90%, we also ran the process optimizations imposing a $CO_2$ recovery constraint of 95% to investigate the effect that a higher recovery has on the ability of MOFs to achieve the targets. The resulting purity/recovery Pareto curves are presented in Figure S17. We see that most of the same materials that met the goals in the previous case were able to meet the goals now, but with a decrease in the purity, which is considerable for the FVSA and the five-step cycle (see Tables S5, S7, and S9). Such a decrease in purity is not desirable for carbon capture, as sometimes the CCS purity requirements are imposed to 95%.[25,38,39]

**Economic Analysis and Comparison with Other Metrics**

The process-level optimization results provide valuable information on the capabilities of the adsorbents to achieve the $CO_2$ purity and recovery goals. However, the economic performance of the adsorbents is quite important for their large-scale applications in CCS. Thus, we carried out an economic analysis on those adsorbents that met purity and recovery targets in the different cycles. In this analysis, we use the adsorbent productivity and energy requirement as proxies for the economic cost. In the economic analysis, the best performing materials have the lowest energy requirements, minimizing the electricity needed to capture the $CO_2$, combined with the highest productivity, minimizing the amount of material needed to capture the $CO_2$ from a given flue gas stream. The results from the economic optimization are shown in Figure 3 (a-c) for the three cycles. In this optimization, we set a constraint that all points have a $CO_2$ purity and recovery above 90%, so that all points meet the CCS goals.

For each cycle, Figure 3 shows a clear difference in the performance of the different MOFs at higher productivities. At low productivity and low energy, the different MOFs appear to converge in their behavior. This is clearly seen in Figure 3a and hinted at in Figures 3b and 3c. For example, Figure 3 shows a common point of low productivity and energy of ~130-140 kWh/ton $CO_2$ for the modified Skarstrom cycle, and ~150-250 kWh/ton $CO_2$ for the five-step cycle. This common low energy

and low productivity point is less perceptible for the FVSA cycle, but it is clear that the energy requirement is significantly higher for this cycle. The optimal decision variables that correspond to the Pareto points in Figure 3 can be found in Tables S10, S12 and S14 for the highest productivities, and in Tables S11, S13 and S15 for the low productivity and low energy points. We can conclude that among the three cycles, the modified Skarstrom cycle and five-step cycle are better choices than the FVSA cycle, as they present the lowest energy requirements for a given productivity. The higher energy consumption in the FVSA could be explained by examining the cycle steps in the three cycle configurations (Figure 1). We can see that the FVSA cycle has two key depressurization steps that contribute more to energy consumption, and even though the five step cycle also has these two depressurization steps, it saves energy by including a light product pressurization step. In addition, the FVSA cycle has the highest $P_H$ values and the lowest depressurization pressures among the three cycles (see Tables S12-S13), which also contribute to the high energy consumption.

To rank the materials based on the economic optimizations, we take advantage of the fact that the fronts for the different materials in Figure 3 are generally parallel to one another. This allows us, conceptually, to start at the lower right corner of each graph and move toward the upper left corner, ranking the materials as we go. In practice, we chose several points along the y-axis in Figure 3 in a range of 250-350 KWh/ton $CO_2$ captured for the modified Skarstrom cycle and the five-step cycle, and 450-550 KWh/ton $CO_2$ captured for the FVSA cycle. We then ranked the materials based on the productivities at these points. Table 3 shows that the ranking is different for each cycle (right 3 columns of Table 3, with best MOFs on the top). However, there are strong similarities. For example, UTSA-16, Cu-TDPAT, and zeolite 13X are the top three performing materials in all 3 cycles.

Table 3 also shows the ranking of the 16 materials according to common metrics used in the literature, namely the working capacity of $CO_2$ (WC), the $CO_2$ selectivity (α), the sorbent selection parameter (S), the adsorbent performance indicator (API), the adsorbent figure of merit (AFM), the separation factor (SF), and the general evaluation metric (GEM). These metrics are defined in Table 4, and the numerical values of the metrics for each material are presented in Table S16. Table 3 shows that in some cases the rankings from the traditional metrics can be misleading. For example, Co-MOF-74 and UiO-66(OH)$_2$ are ranked among the top 7 materials by the WC and API$_2$ although these MOFs are not able to achieve the $CO_2$ purity and recovery requirements as demonstrated in the process-level modeling and optimization. Among the derived metrics used in this work, only the GEM is able to predict the top three performing materials according to the economic ranking of the different PSA cycles. This reflects the fact that the GEM was trained and derived based on economic process optimization.[21]

Nonetheless, most metrics identified some materials that perform well for carbon capture. For example, SIFSIX-3-Ni was ranked as the top performing material by several metrics, and this material is among the top 7 for all three of the studied cycles. Similarly, UTSA-16, Cu-TDPAT, and zeolite 13X, which were the top

performing materials in the three cycles, were included in the top 7 materials according to many of the derived metrics. Also, the metrics, in general, are good at identifying the low-performing materials such as MOF-177 and ZIF-8. In summary, we can say that the derived metrics in the literature can be useful but should be used carefully, and process optimizations should still be included in the evaluation of adsorbent performance when possible. Testing of the simple metrics on larger sets of adsorbents would be an interesting topic for further study.

**Connecting Material Properties and Process Performance**

UTSA-16, Cu-TDPAT, Zn-MOF-74, Ti-MIL-91, and SIFSIX-3-Ni are predicted to meet the purity and recovery targets for all three cycles considered in this work. We examined their material properties and isotherms and compared them to lower performing materials to better understand what material properties lead to good performance in $CO_2$ capture. Table 1 shows that the top performing MOFs all have surface areas lower than 1200 $m^2$/g with the exception of Cu-TDPAT, which has a surface area of 1940 $m^2$/g. Surface area is usually loosely correlated with pore size, but the correlation between surface area or pore size and $CO_2$ adsorption is not straightforward.[19] The good performance of Cu-TDPAT could be related to its small pores (largest cavity diameter, LCD = 5.3 Å) and to the large difference between the heats of adsorption of $CO_2$ and $N_2$ ($\Delta Q_{st}^0$ = 23 kJ/mol). The other top performing MOFs, UTSA-16, Ti-MIL-91, and SIFSIX-3-Ni also have low LCD and high $\Delta Q_{st}^0$. The various forms of MOF-74 considered here have larger pores than most of the other MOFs in Table 1, but they have high $\Delta Q_{st}^0$, which lead to generally good performance. All of the poor performing MOFs have either a high surface area and/or a high LCD and/or a low $\Delta Q_{st}^0$.

The $CO_2$ and $N_2$ isotherms for the top performing MOFs UTSA-16, Cu-TDPAT, Zn-MOF-74, Ti-MIL-91, and SIFSIX-3-Ni along with zeolite 13X are plotted in Figure 4. For comparison, the isotherms for six of the worst performing materials (Co-MOF-74, Cu-BTTRi, NTU-105, MOF-177, ZIF-8, and $Sc_2BDC_3$) are shown in Figure 5. The materials in Figure 4 generally show higher $CO_2$ uptake and lower $N_2$ uptake than those in Figure 5. However, the shape of the isotherm also plays a role, especially in determining the working capacity. We define the working capacity in this work as

$$WC_i = N_{ads,i} - N_{des,i} \qquad (11)$$

where $N_{ads,i}$ and $N_{des,i}$ are the uptake of component $i$ at specified adsorption and desorption conditions, respectively. The desorption loading was calculated for a 90:10 $CO_2$:$N_2$ stream at 0.1 bar and 313 K, which is representative of the outlet stream in a VSA process. For the adsorption loading, we calculated the working capacity for two streams. First, we considered the flue gas feed with a composition of 15:85 $CO_2$:$N_2$ at 1 bar and 313 K. Second, we looked at a 90:10 $CO_2$:$N_2$ stream under the same pressure and temperature, since the $CO_2$ gas-phase mole fraction in the column could increase due to the heavy reflux step included in two of the cycles. The working capacities are given in Table 5 along with the selectivities for the top six materials. Among the top materials, SIFSIX-3-Ni has the highest selectivity but shows a much lower $CO_2$ working

capacity than the other materials, especially for the 90:10 $CO_2$:$N_2$ adsorption conditions. The low working capacity of SIFSIX-3-Ni is due to the steepness of its $CO_2$ isotherm at low pressures and leads to the relatively low performance of SIFSIX-3-Ni in the process economics modeling (Table 3 right columns). The steep isotherm of SIFSIX-3-Ni is in contrast to the top two performing MOFs UTSA-16 and Cu-TDPAT, which have a high $CO_2$ uptake at 1 bar, with a gradual increase in the $CO_2$ uptake over the pressure range. Although the $CO_2$ working capacity of a material should be directly related to the amount of $CO_2$ that a given mass of adsorbent can cycle through over a given time, it can be seen that Zn-MOF-74 has a $CO_2$ working capacity around 35% higher than Cu-TDPAT, but looking at the ranking based on the three cycles in Table 3, Cu-TDPAT outperformed Zn-MOF-74, indicating that the use of only the working capacity to identify the best materials is not sufficient.

**SIFSIX-3-Ni Analysis**

Five of the metrics considered in this work predicted SIFSIX-3-Ni to be the top performing material. It shows the highest $CO_2$/$N_2$ selectivity, and it is a highly stable MOF with a relatively easy and scalable synthesis procedure, which are important for large-scale application. Since the experimental $N_2$ heat of adsorption for this MOF was not available in the literature, we synthesized it and performed variable-temperature isotherm measurements for $CO_2$ and $N_2$.

The sorption isotherms for SIFSIX-3-Ni are reported in Tables S17-S21 and plotted in Figure S18 along with the fitted isotherms. With the sorption data at different temperatures collected in this work, we estimated a $N_2$ heat of adsorption of 21 kJ/mol. Note that this value differs from the value initially assumed of 12 kJ/mol for some MOFs, including SIFSIX-3-Ni, when experimental data were unavailable. This value is also beyond the range used in the sensitivity analysis presented in the supplementary material (6-18 kJ/mol). Although all results presented in this work for SIFSIX-3-Ni are based on the experimental $N_2$ heat of adsorption, we compared the productivity/energy Pareto curves of SIFSIX-3-Ni using the assumed value and the experimental one to measure the effect that the $N_2$ heat of adsorption has on the economic results. Thus, Figure 6 shows the energy/productivity Pareto fronts for SIFSIX-3-Ni with $N_2$ heats of adsorption of 12 and 21 kJ/mol. There is a small but clear difference in the curves for all three cycles using a value of 21 kJ/mol versus 12 kJ/mol, which seems to be greater at higher productivities. This result suggests that the optimal energy/productivity Pareto fronts presented for Cu-TDPAT, Zn-MOF-74, and SIFSIX-2-Cu-i could shift somewhat if more accurate values of $N_2$ heat of adsorption are used, but the general trends and rankings are unlikely to change.

Another point to highlight is that SIFSIX-3-Ni does not present very different values for the heats of adsorption of $CO_2$ (35 kJ/mol) and $N_2$ (21 kJ/mol), although it is commonly accepted in the literature that high $CO_2$ selectivity is favored by a large difference of the isosteric heats of adsorption of $CO_2$ and $N_2$.[18] This could be a possible reason to explain the relatively poor position of SIFSIX-3-Ni in the ranking from the different PSA cycles compared to other top performing MOFs such as UTSA-16 and Cu-TDPAT which exhibit higher differences in the heats of adsorption of the two components. We note that

another MOF with a small difference in the isosteric heats of adsorption of $CO_2$ and $N_2$ is Mg-MOF-74, which has similar performance and ranking as SIFSIX-3-Ni.

## Conclusions

In this work, we selected 15 MOFs that were reported in the literature as promising candidates for carbon capture applications and tested them using process-level modelling of three pressure-swing adsorption cycles: a modified Skarstrom cycle, a fractionated vacuum swing adsorption (FVSA) cycle, and a five-step cycle. For each cycle we conducted both process-level optimization and economic-level analysis. From the process-level analysis, we found that only 8 of the examined MOFs were able to achieve a $CO_2$ purity and recovery of 90% (the DOE goals for CCS) for the modified Skarstrom cycle; 5 for the FVSA cycle; and 6 for the five-step cycle. Zeolite 13X met the purity and recovery targets in all cycles. Economic analysis was then conducted on the MOFs able to achieve the purity and recovery targets by examining the tradeoff between productivity and energy requirement. From these results, the modified Skarstrom cycle and the five step cycle were found to have lower energy requirements for a given productivity compared to the FVSA cycle. Based on the economic optimization results, the following MOFs were predicted to be the most promising for carbon capture among the materials studied here: UTSA-16, Cu-TDPAT, Zn-MOF-74, Ti-MIL-91, and SIFSIX-3-Ni. Based on this small data set, the top materials tend to have high $CO_2$ working capacity, small pore diameter, and a large difference between the heats of adsorption of $CO_2$ and $N_2$. Rankings from PSA modeling were compared to those using simple sorbent evaluation metrics from the literature. We found that the metrics in the literature can be useful as a pre-screening filter for identifying materials from large data sets but should be used carefully, and PSA process optimization should still be included in the evaluations of adsorbent performance when possible.

## Acknowledgements

## References

1    P. A. Webley, *Adsorption*, 2014, **20**, 225–231.

2    D. M. Ruthven, S. Farooq and K. S. Knaebel, *Pressure swing adsorption*, VCH Publishers, New York, NY, 1994.

3    J. Jiang, H. Furukawa, Y.-B. Zhang and O. M. Yaghi, *Journal of the American Chemical Society*, 2016, **138**, 10244–10251.

4    H. Zhang, P. Deria, O. K. Farha, J. T. Hupp and R. Q. Snurr, *Energy Environ. Sci.*, 2015, **8**, 1501–1510.

5    Z. R. Herm, B. M. Wiers, J. A. Mason, J. M. van Baten, M. R. Hudson, P. Zajdel, C. M. Brown, N. Masciocchi, R. Krishna and J. R. Long, *Science*, 2013, **340**, 960–964.

6    A. E. Platero-Prats, Z. Li, L. C. Gallington, A. W. Peters, J. T. Hupp, O. K. Farha and K. W. Chapman, *Faraday Discuss.*, 2017, **201**, 337–350.

7    D. Britt, C. Lee, F. J. Uribe-Romo, H. Furukawa and O. M. Yaghi, *Inorganic Chemistry*, 2010, **49**, 6387–6389.

8    G. Wang, C. Sharp, A. M. Plonka, Q. Wang, A. I. Frenkel, W. Guo, C. Hill, C. Smith, J. Kollar, D. Troya and J. R. Morris, *The Journal of Physical Chemistry C*, 2017, **121**, 11261–11272.

9    K. O. Kirlikovali, Z. Chen, T. Islamoglu, J. T. Hupp and O. K. Farha, *ACS Applied Materials & Interfaces*, 2020, **12**, 14702–14720.

10   M. Ding, R. W. Flaig, H.-L. Jiang and O. M. Yaghi, *Chem. Soc. Rev.*, 2019, **48**, 2783–2828.

11   B. J. Maring and P. A. Webley, *International Journal of Greenhouse Gas Control*, 2013, **15**, 16–31.

12   A. Ö. Yazaydın, R. Q. Snurr, T.-H. Park, K. Koh, J. Liu, M. D. LeVan, A. I. Benin, P. Jakubczak, M. Lanuza, D. B. Galloway, J. J. Low and R. R. Willis, *Journal of the American Chemical Society*, 2009, **131**, 18198–18199.

13   R. Krishna, *RSC Adv.*, 2017, **7**, 35724–35737.

14   S. U. Rege and R. T. Yang, *Separation Science and Technology*, 2001, **36**, 3355–3365.

15   F. Notaro, J. T. Mullhaupt, F. W. Leavitt, M. W. Ackley. Adsorption process and system using multilayer adsorbent beds. U.S. Patent #5810909, September 1998.

16   A. D. Wiersum, J.-S. Chang, C. Serre and P. L. Llewellyn, *Langmuir*, 2013, **29**, 3301–3309.

17   G. D. Pirngruber, L. Hamon, S. Bourrelly, P. L. Llewellyn, E. Lenoir, V. Guillerm, C. Serre and T. Devic, *ChemSusChem*, 2012, **5**, 762–776.

18   D. Wu, Q. Yang, C. Zhong, D. Liu, H. Huang, W. Zhang and G. Maurin, *Langmuir*, 2012, **28**, 12094–12099.

19   C. E. Wilmer, O. K. Farha, Y.-S. Bae, J. T. Hupp and R. Q. Snurr, *Energy Environ. Sci.*, 2012, **5**, 9849–9856.

20   C. Altintas, G. Avci, H. Daglar, A. Nemati Vesali Azar, S. Velioglu, I. Erucar and S. Keskin, *ACS Applied Materials & Interfaces*, 2018, **10**, 17257–17268.

21   K. T. Leperi, Y. G. Chung, F. You and R. Q. Snurr, *ACS Sustainable Chemistry & Engineering*, 2019, **7**, 11529–11539.

22   V. Subramanian Balashankar, A. K. Rajagopalan, R. de Pauw, A. M. Avila and A. Rajendran, *Industrial & Engineering Chemistry Research*, 2019, **58**, 3314–3328.

23   D. W. Siderius, V. K. Shen, R. D. Johnson III and R. D. van Zee, *NIST/ARPA-E Database of Novel and Emerging Adsorbent Materials*, National Institute of Standards and Technology, Gaithersburg MD, 2017; https://dx.doi.org/10.18434/T43882.

24   A. K. Rajagopalan, A. M. Avila and A. Rajendran, *International Journal of Greenhouse Gas Control*, 2016, **46**, 76–85.

25   M. Khurana and S. Farooq, *Industrial & Engineering Chemistry Research*, 2016, **55**, 2447–2460.

26   D. Danaci, M. Bui, N. Mac Dowell and C. Petit, *Mol. Syst. Des. Eng.*, 2020, **5**, 212–231.

27   V. Subramanian Balashankar and A. Rajendran, *ACS Sustainable Chemistry & Engineering*, 2019, **7**, 17747–17755.

28   A. H. Farmahini, D. Friedrich, S. Brandani and L. Sarkisov, *Energy Environ. Sci.*, 2020, **13**, 1018–1037.

29   R. Haghpanah, A. Majumder, R. Nilam, A. Rajendran, S. Farooq, I. A. Karimi and M. Amanullah, *Industrial & Engineering Chemistry Research*, 2013, **52**, 4249–4265.

30   R. Haghpanah, R. Nilam, A. Rajendran, S. Farooq and I. A. Karimi, *AIChE Journal*, 2013, **59**, 4735–4748.

31   K. T. Leperi, R. Q. Snurr and F. You, *Industrial & Engineering Chemistry Research*, 2016, **55**, 3338–3350.

32   G.-S. Jiang and C.-W. Shu, *Journal of Computational Physics*, 1996, **126**, 202–228.

33   L. Shampine and M. Reichelt, *SIAM Journal on Scientific Computing*, 1997, **18**, 1–22.

34   S. P. Reynolds, A. Mehrotra, A. D. Ebner and J. A. Ritter, *Adsorption*, 2008, **14**, 399–413.

35   K. Deb, A. Pratap, S. Agarwal and T. Meyarivan, *IEEE Transactions on Evolutionary Computation*, **6**, 182–197.

36   H. K. Chae, D. Y. Siberio-Pérez, J. Kim, Y. Go, M. Eddaoudi, A. J. Matzger, M. O'Keeffe, O. M. Yaghi, M. Design and D. Group, *Nature*, 2004, **427**, 523–527.

37   X.-J. Wang, P.-Z. Li, Y. Chen, Q. Zhang, H. Zhang, X. X. Chan, R. Ganguly, Y. Li, J. Jiang and Y. Zhao, *Scientific reports*, 2013, **3**, 1149–1149.

38   K. N. Pai, J. D. Baboolal, D. A. Sharp and A. Rajendran, *Separation and Purification Technology*, 2019, **211**, 540–550.

39   N. Susarla, R. Haghpanah, I. A. Karimi, S. Farooq, A. Rajendran, L. S. C. Tan and J. S. T. Lim, *Chemical Engineering Research and Design*, 2015, **102**, 354–367.

40   H.-Y. Cho, D.-A. Yang, J. Kim, S.-Y. Jeong and W.-S. Ahn, *Catalysis Today*, 2012, **185**, 35–40.

41   A. Demessence, D. M. D'Alessandro, M. L. Foo and J. R. Long, *Journal of the American Chemical Society*, 2009, **131**, 8784–8786.

42   Z. Zhang, Z. Li and J. Li, *Langmuir*, 2012, **28**, 12122–12133.

43   J. A. Mason, K. Sumida, Z. R. Herm, R. Krishna and J. R. Long, *Energy Environ. Sci.*, 2011, **4**, 3030–3040.

44   T.-H. Bae and J. R. Long, *Energy Environ. Sci.*, 2013, **6**, 3565–3569.

45   D. Yu, A. O. Yazaydin, J. R. Lane, P. D. C. Dietzel and R. Q. Snurr, *Chem. Sci.*, 2013, **4**, 3544–3556.

46   X.-J. Wang, P.-Z. Li, Y. Chen, Q. Zhang, H. Zhang, X. X. Chan, R. Ganguly, Y. Li, J. Jiang and Y. Zhao, *Scientific Reports*, 2013, **3**, 1149.

47   R. S. Pillai, V. Benoit, A. Orsi, P. L. Llewellyn, P. A. Wright and G. Maurin, *The Journal of Physical Chemistry C*, 2015, **119**, 23592–23598.

48   P. Nugent, Y. Belmabkhout, S. D. Burd, A. J. Cairns, R. Luebke, K. Forrest, T. Pham, S. Ma, B. Space, L. Wojtas, M. Eddaoudi and M. J. Zaworotko, *Nature*, 2013, **495**, 80–84.

49   V. Benoit, R. S. Pillai, A. Orsi, P. Normand, H. Jobic, F. Nouar, P. Billemont, E. Bloch, S. Bourrelly, T. Devic, P. A. Wright, G. de Weireld, C. Serre, G. Maurin and P. L. Llewellyn, *J. Mater. Chem. A*, 2016, **4**, 1383–1389.

50   A. Masala, J. G. Vitillo, G. Mondino, C. A. Grande, R. Blom, M. Manzoli, M. Marshall and S. Bordiga, *ACS Applied Materials & Interfaces*, 2017, **9**, 455–463.

51   S. Xiang, Y. He, Z. Zhang, H. Wu, W. Zhou, R. Krishna and B. Chen, *Nature Communications*, 2012, **3**, 954.

52   Z. Hu, Y. Wang, S. Farooq and D. Zhao, *AIChE Journal*, 2017, **63**, 4103–4114.

53   Z. Zhang, S. Xian, Q. Xia, H. Wang, Z. Li and J. Li, *AIChE Journal*, 2013, **59**, 2195–2206.

54   S. Krishnamurthy, V. R. Rao, S. Guntuka, P. Sharratt, R. Haghpanah, A. Rajendran, M. Amanullah, I. A. Karimi and S. Farooq, *AIChE Journal*, 2014, **60**, 1830–1842.

55   T. F. Willems, C. H. Rycroft, M. Kazi, J. C. Meza and M. Haranczyk, *Microporous and Mesoporous Materials*, 2012, **149**, 134–141.

## Tables

Table 1. MOFs investigated in this study along with structural properties and references for the experimental $CO_2$ and $N_2$ isotherms and heats of adsorption.

| MOF | BET Area (m²/g) | Pore Volume (cm³/g) | PLD (Å) | LCD (Å) | $Q_{st}^0$ (kJ/mol) CO₂ | N₂ | Isotherm Reference |
|---|---|---|---|---|---|---|---|
| Co-MOF-74 | 1325 | 0.52 | 10.8 | 11.5 | 35 | 19 | Cho *et al.*[40] |
| Cu-BTTRi | 1770 | 0.71 | 10.5 | 11.3 | 25 | 6 | Demessence *et al.*[41] |
| Cu-TDPAT | 1940 | 0.93 | 3.6 | 5.3 | 35 | 12 | Zhang *et al.*[42] |
| Mg-MOF-74 | 1640 | 0.57 | 11.1 | 11.9 | 36 | 13 | Marring *et al.*[11] |
| MOF-177 | 4690 | 1.59 | 9.9 | 11.2 | 14 | 10 | Mason *et al.*[43] |
| Ni-MOF-74 | 1220 | 0.48 | 10.7 | 11.5 | 38 | 14 | Bae and Long[44] and Yu *et al.*[45] |
| NTU-105 | 3545 | 1.33 | 6.9 | 18.5 | 26 | 12 | Wang *et al.*[46] |
| Sc₂BDC₃ | 595 | 0.25 | 3.0 | 4.0 | 27 | 18 | Pillai *et al.*[47] |
| SIFSIX-2-Cu-i | 735 | 0.26 | 3.8 | 4.8 | 32 | 12 | Nugent *et al.*[48] |
| SIFSIX-3-Ni | 365 | 0.15 | 3.1 | 3.9 | 35 | 21 | This work |
| Ti-MIL-91 | 380 | 0.14 | 3.6 | 4.7 | 42 | 19 | Benoit *et al.*[49] |
| UTSA-16 | 625 | 0.31 | 4.2 | 7.2 | 41 | 12 | Masala *et al.*[50] and Xiang *et al.*[51] |
| UiO-66(OH)₂ | 1230 | 0.56 | 3.8 | 8.9 | 30 | 13 | Hu *et al.*[52] |
| ZIF-8 | 1025 | 0.54 | 3.4 | 11.4 | 19 | 10 | Zhang *et al.*[53] |
| Zn-MOF-74 | 1175 | 0.58 | 11.1 | 11.9 | 30 | 12 | Xiang *et al.*[51] |
| Zeolite 13X | 685 | 0.30 | 7.0 | 11.0 | 36 | 16 | Krishnamurthy *et al.*[54] |

BET area and pore volume were taken from the isotherm references. Pore-limiting diameter (PLD) and largest cavity diameter (LCD) of adsorbents were estimated using the Zeo++ software.[55]

Table 2. Decision variables with bounds used in process and economic optimizations for the different PSA cycles

| | L [m] | $P_H$ [bar] | $P_L$ [bar] | $P_I$ [bar] | $t_{feed}$ [s] | $v_{feed}$ [m/s] | $\alpha_{LR}^*$ [-] | $\alpha_{HR}^{**}$ [-] |
|---|---|---|---|---|---|---|---|---|
| Modified Skarstrom cycle | $1-7$ | $1-10$ | $0.1-0.5$ | $-$ | $10-1000$ | $0.1-2$ | $0.01-0.99$ | $0-1$ |
| FVSA cycle | $1-7$ | $1-10$ | $0.1-0.5$ | $0.11-3$ | $10-1000$ | $0.1-2$ | $-$ | $-$ |
| Five Step Cycle | $1-7$ | $1-10$ | $0.1-0.5$ | $0.11-3$ | $10-1000$ | $0.1-2$ | $-$ | $0-1$ |

$^*$ light reflux ratio (fraction of the light product in the adsorption step that is sent to the light reflux step), $^{**}$ heavy reflux ratio (fraction of the heavy product in the light reflux step or the counter-current depressurization step that is sent to the heavy reflux step)

Table 3. Ranking of materials using some traditional metrics and using economic level process optimization for three cycle configurations*

| | WC | α | S | API₁ | API₂ | AFM₁ | AFM₂ | SF | GEM | Mod. Skars. | 5-Step Cycle | FVSA |
|---|---|---|---|---|---|---|---|---|---|---|---|---|
| 1 | Ni-MOF-74 | SIFSIX-3-Ni | SIFSIX-3-Ni | Mg-MOF-74 | Mg-MOF-74 | SIFSIX-3-Ni | SIFSIX-3-Ni | SIFSIX-3-Ni | UTSA-16 | Zeolite 13X | UTSA-16 | Cu-TDPAT |
| 2 | Mg-MOF-74 | Zeolite 13X | Zeolite 13X | Zeolite 13X | Ni-MOF-74 | Zeolite 13X | Zeolite 13X | UTSA-16 | Cu-TDPAT | Cu-TDPAT | Zeolite 13X | UTSA-16 |
| 3 | Co-MOF-74 | Mg-MOF-74 | UTSA-16 | SIFSIX-3-Ni | UTSA-16 | Mg-MOF-74 | UTSA-16 | Zeolite 13X | Zeolite 13X | UTSA-16 | Cu-TDPAT | Zeolite 13X |
| 4 | UiO-66(OH)₂ | UTSA-16 | Cu-TDPAT | Ni-MOF-74 | Zeolite 13X | Ni-MOF-74 | Cu-TDPAT | Ni-MOF-74 | SIFSIX-3-Ni | Ni-MOF-74 | Ti-MIL-91 | Zn-MOF-74 |
| 5 | UTSA-16 | Cu-TDPAT | Ni-MOF-74 | UTSA-16 | SIFSIX-2-Cu-i | UTSA-16 | Ni-MOF-74 | Cu-TDPAT | Ti-MIL-91 | Mg-MOF-74 | Zn-MOF-74 | Ti-MIL-91 |
| 6 | SIFSIX-2-Cu-i | Ni-MOF-74 | Mg-MOF-74 | Cu-TDPAT | Co-MOF-74 | Cu-TDPAT | Mg-MOF-74 | Ti-MIL-91 | Zn-MOF-74 | SIFSIX-2-Cu-i | SIFSIX-3-Ni | SIFSIX-3-Ni |
| 7 | Zn-MOF-74 | Ti-MIL-91 | Ti-MIL-91 | SIFSIX-2-Cu-i | UiO-66(OH)₂ | SIFSIX-2-Cu-i | Ti-MIL-91 | Mg-MOF-74 | SIFSIX-2-Cu-i | SIFSIX-3-Ni | Mg-MOF-74 | |
| 8 | Zeolite 13X | SIFSIX-2-Cu-i | SIFSIX-2-Cu-i | Zn-MOF-74 | Zn-MOF-74 | Zn-MOF-74 | SIFSIX-2-Cu-i | SIFSIX-2-Cu-i | Ni-MOF-74 | Zn-MOF-74 | | |
| 9 | Cu-TDPAT | Zn-MOF-74 | Zn-MOF-74 | UiO-66(OH)₂ | Cu-TDPAT | Ti-MIL-91 | Zn-MOF-74 | Zn-MOF-74 | Sc2BDC3 | Ti-MIL-91 | | |
| 10 | Ti-MIL-91 | Sc2BDC3 | Sc2BDC3 | Ti-MIL-91 | Ti-MIL-91 | UiO-66(OH)₂ | Sc2BDC3 | Sc2BDC3 | Mg-MOF-74 | | | |
| 11 | Cu-BTTRi | UiO-66(OH)₂ | UiO-66(OH)₂ | Co-MOF-74 | SIFSIX-3-Ni | Co-MOF-74 | UiO-66(OH)₂ | UiO-66(OH)₂ | Cu-BTTRi | | | |
| 12 | NTU-105 | Co-MOF-74 | Co-MOF-74 | Cu-BTTRi | Cu-BTTRi | Cu-BTTRi | Co-MOF-74 | Co-MOF-74 | UiO-66(OH)₂ | | | |
| 13 | SIFSIX-3-Ni | Cu-BTTRi | Cu-BTTRi | NTU-105 | NTU-105 | NTU-105 | Cu-BTTRi | Cu-BTTRi | ZIF-8 | | | |
| 14 | MOF-177 | NTU-105 | NTU-105 | Sc2BDC3 | MOF-177 | Sc2BDC3 | NTU-105 | NTU-105 | Co-MOF-74 | | | |
| 15 | ZIF-8 | ZIF-8 | ZIF-8 | MOF-177 | Sc2BDC3 | MOF-177 | ZIF-8 | ZIF-8 | NTU-105 | | | |
| 16 | Sc2BDC3 | MOF-177 | MOF-177 | ZIF-8 | ZIF-8 | ZIF-8 | MOF-177 | MOF-177 | MOF-177 | | | |

* Working capacity of $CO_2$ (WC), Selectivity (α), Sorbent Selection Parameter (S), Adsorbent Performance Indicator (API₁ and API₂), Adsorbent Figure of Merit (AFM₁ and AFM₂), Separation Factor (SF), General Evaluation Metric (GEM)

Table 4. Traditional metrics used in literature to evaluate the performance of adsorbent materials[*]

| Adsorbent Metric | Definition | Reference |
|---|---|---|
| PSA Sorbent Selection Parameter | $S = \alpha_{ads}\dfrac{WC_1}{WC_2}$ | Rege and Yang[14] |
| Adsorbent Performance Indicator | $API_1 = \dfrac{(\alpha_{ads} - 1)WC_1}{\lvert \Delta H_{ads,1} \rvert}$ | Wiersum et al.[16] |
| Adsorbent Performance Indicator | $API_2 = \dfrac{(\alpha_{ads} - 1)^{0.5}WC_1{}^2}{\lvert \Delta H_{ads,1} \rvert}$ | Wiersum et al.[16] |
| Adsorbent Figure of Merit | $AFM_1 = WC_1\dfrac{\alpha_{ads}^2}{\alpha_{des}}$ | Notaro et al.[15] |
| Adsorbent Figure of Merit | $AFM_2 = \dfrac{WC_1\alpha_{ads}^2}{WC_2\alpha_{des}}$ | Rege and Yang[14] |
| Separation Factor | $SF = \dfrac{WC_1}{WC_2}\dfrac{y_2}{y_1}$ | Pirngruber et al.[17] |
| General Evaluation Metric | $GEM = \dfrac{WC_1}{WC_{2,mod}{}^{1.32} \cdot \alpha_{des}{}^{0.25} \lvert \Delta H_{ads,2} \rvert^{0.97}}$ | Leperi et al.[21] |

[*] Subscripts 1 and 2 represent component 1 ($CO_2$) and component 2 ($N_2$). The working capacities, WC, are defined in eq. (10). $\alpha_{ads}$ is the selectivity at adsorption conditions for component 1 over component 2, which was calculated considering a gas stream of 15:85 $CO_2$:$N_2$ at 1 bar and 313 K. $\alpha_{des}$ is the selectivity at desorption conditions for component 1 over component 2, which was calculated considering a gas stream of 90:10 $CO_2$:$N_2$ at 0.1 bar and 313 K. $WC_{2,\,mod}$ is defined as max($WC_2$, 0.01). The mole fraction of component $i$ in the gas phase is denoted $y_i$.

Table 5. Working capacities and selectivities of top six adsorbents.

| Adsorbent | $WC_{CO2}$ [mol/kg][*] | $WC_{CO2}$ [mol/kg][**] | Selectivity$_{CO2}$[***] |
|---|---|---|---|
| UTSA-16 | 0.49 | 2.60 | 246 |
| Zn-MOF-74 | 0.40 | 3.30 | 63 |
| Zeolite 13X | 0.32 | 1.51 | 61 |
| Cu-TDPAT | 0.26 | 2.61 | 214 |
| Ti-MIL-91 | 0.21 | 1.78 | 92 |
| SIFSIX-3-Ni | 0.10 | 0.46 | 2848 |

[*]working capacity under adsorption conditions with a gas composition of 15% $CO_2$ and 85% $N_2$ at 1 bar pressure and 313 K. [**]working capacity under adsorption conditions with a gas composition of 90% $CO_2$ and 10% $N_2$ at 1 bar pressure and 313 K. Desorption conditions are based on a gas composition of 90% $CO_2$ and 10% $N_2$ at 0.1 bar pressure and 313 K in all cases. [***] selectivity of $CO_2$ is calculated under adsorption conditions with a gas stream of 15:85 $CO_2$:$N_2$ at 1 bar and 313 K.

# Figures
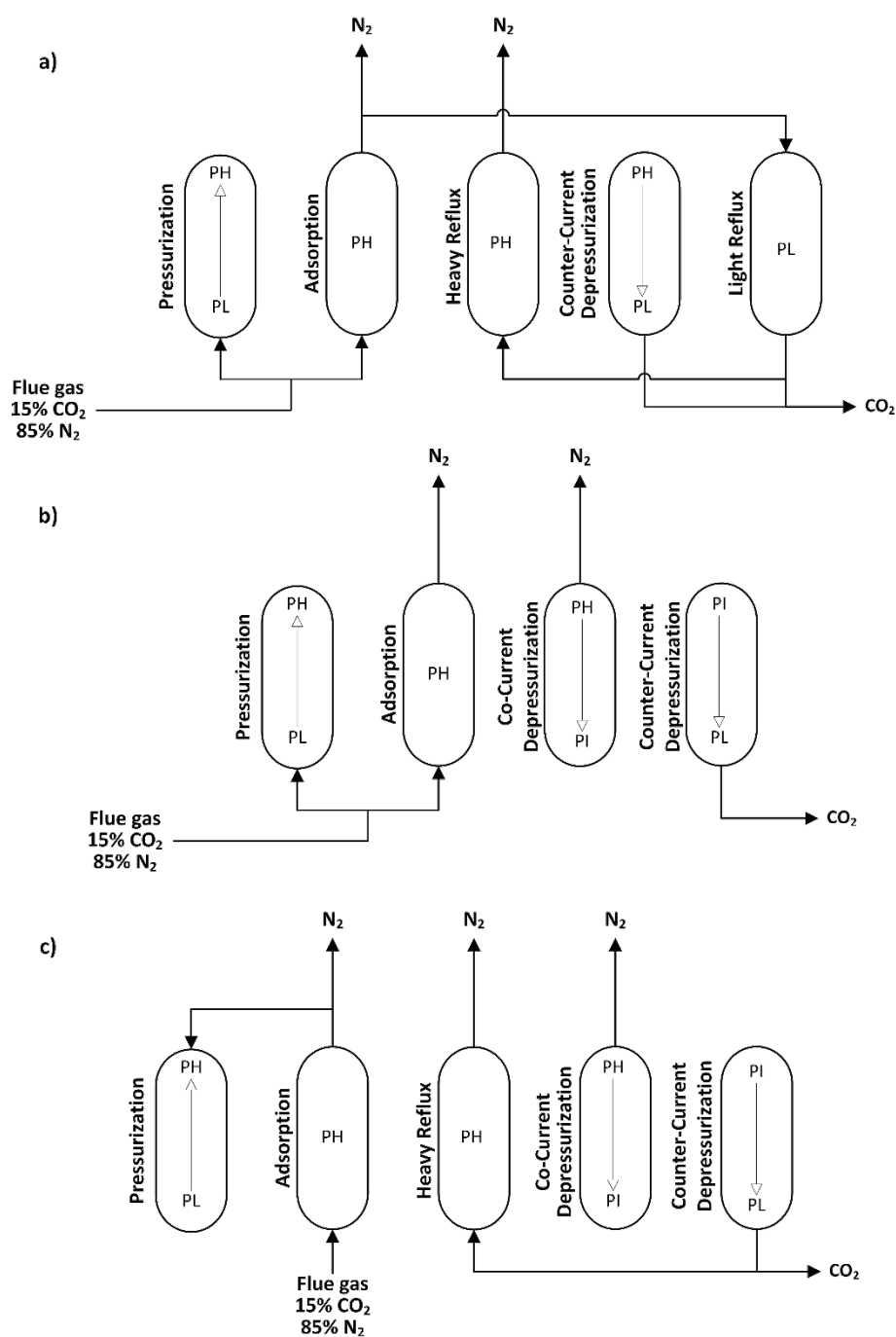


Figure 1. Schematics of the (a) modified Skarstrom cycle, (b) FVSA cycle, and (c) five-step cycle used in this study. Note that each schematic displays the ordering of the steps for a single column. So, one column first runs the pressurization step, followed by the adsorption step, etc.
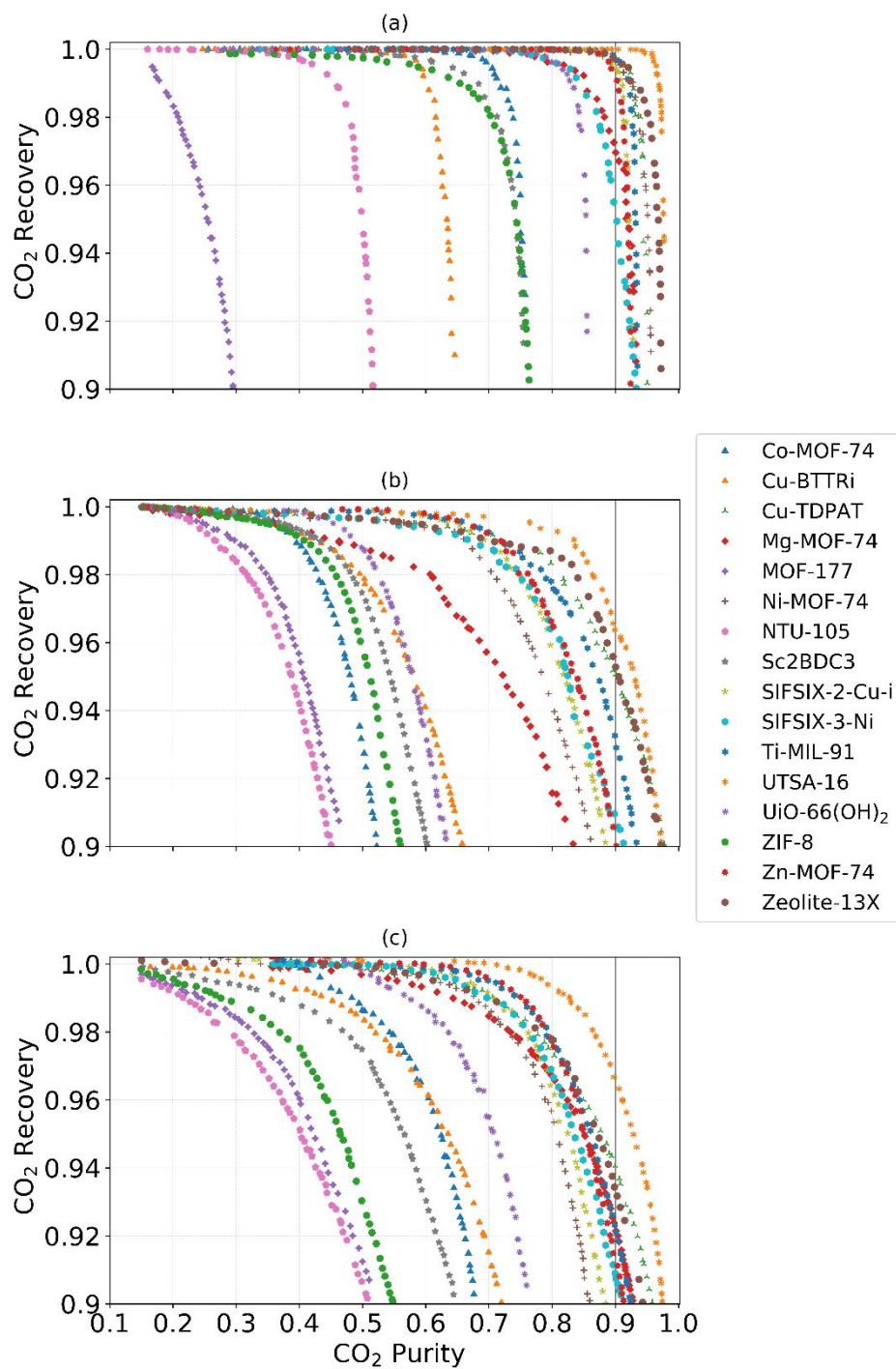
Figure 2. Purity / Recovery Pareto fronts for the 15 MOFs and zeolite 13X. (a) Modified Skarstrom cycle. (b) Fractionated vacuum swing adsorption cycle (FVSA). (c) five-step cycle. Of the 16 adsorbents tested, only 9 were able to achieve the DOE's goals for $CO_2$ capture (90% purity and 90% recovery) for the modified Skarstrom cycle, only 6 for the FVSA, and only 7 for the five-step cycle.
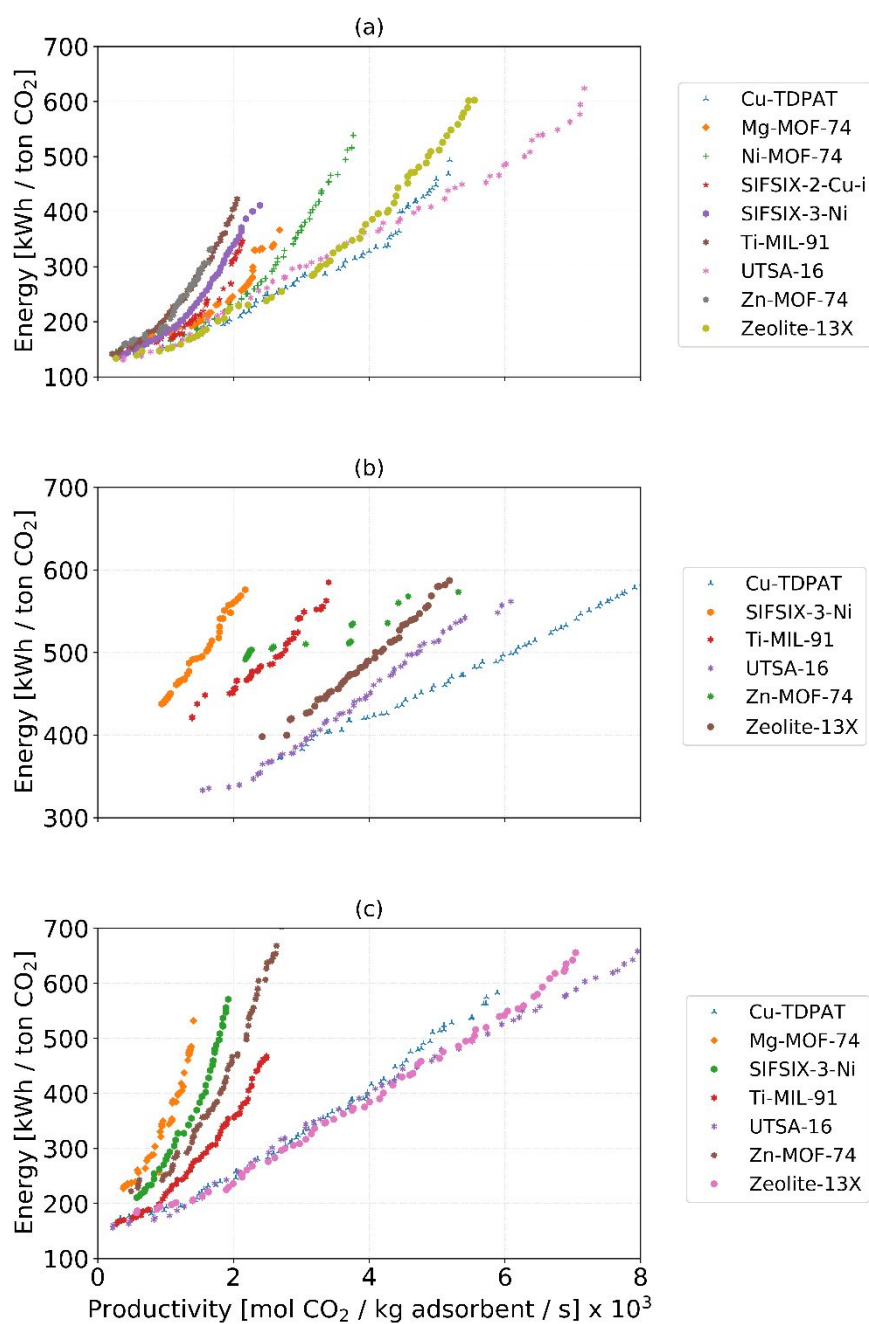
Figure 3. The energy / productivity Pareto fronts for the adsorbents capable of achieving the DOE's purity and recovery goals for each cycle. a) Modified Skarstrom cycle, b) fractionated vacuum swing adsorption cycle (FVSA), c) five-step cycle.
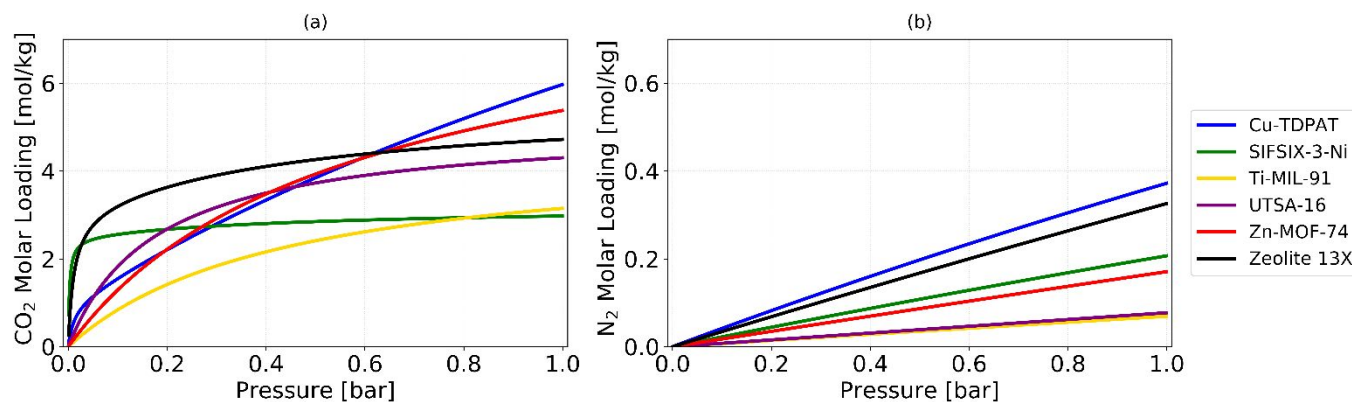
Figure 4. Pure component isotherms of the six top performing materials for (a) $CO_2$ and (b) $N_2$ at 313 K.
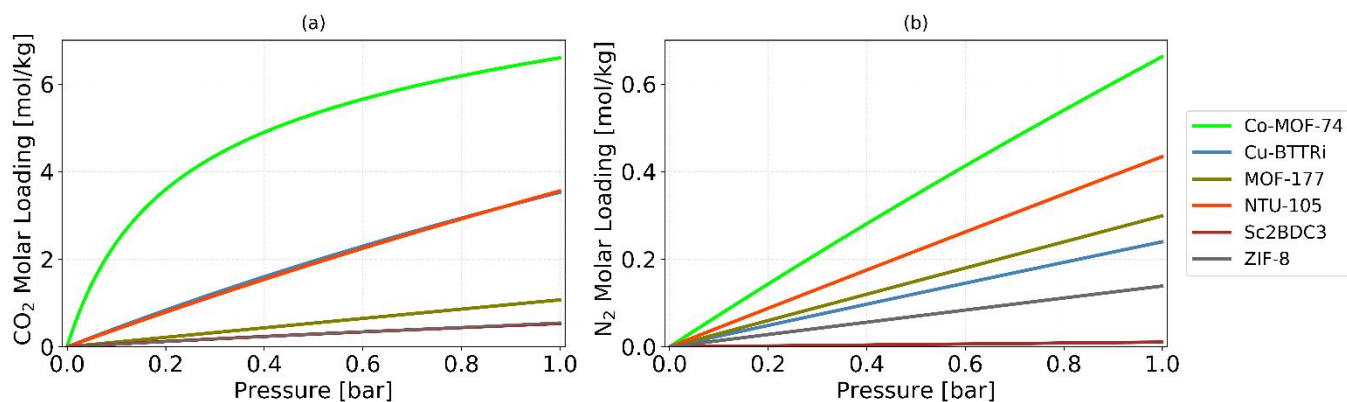


Figure 5. Pure component isotherms of six of the worst performing materials for (a) $CO_2$ and (b) $N_2$ at 313 K.
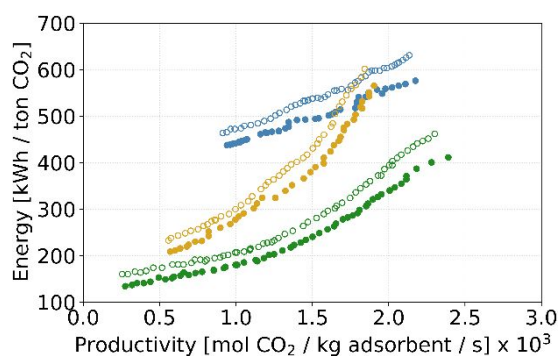


Figure 6. Comparison of the energy/productivity Pareto fronts for SIFSIX-3-Ni with $N_2$ heat of adsorption of 12 kJ/mol (open symbols) and 21 kJ/mol (closed symbols) for the modified Skarstrom cycle (green), the FVSA cycle (yellow), and the five step cycle (blue).

Table of Contents Graphic